Macro Domain from Middle East Respiratory Syndrome Coronavirus (MERS-CoV) Is an Efficient ADP-ribose Binding Module

CRYSTAL STRUCTURE AND BIOCHEMICAL STUDIES[*]

Chao-Cheng Cho[‡], Meng-Hsuan Lin[‡], Chien-Ying Chuang[§¶], and Chun-Hua Hsu[‡§¶1]

From the [‡]Genome and Systems Biology Degree Program, National Taiwan University and Academia Sinica, Taipei 10617, the [§]Department of Agricultural Chemistry, National Taiwan University, Taipei 10617, and the [¶]Center for Systems Biology, National Taiwan University, Taipei 10617, Taiwan

The newly emerging Middle East respiratory syndrome coronavirus (MERS-CoV) encodes the conserved macro domain within non-structural protein 3. However, the precise biochemical function and structure of the macro domain is unclear. Using differential scanning fluorimetry and isothermal titration calorimetry, we characterized the MERS-CoV macro domain as a more efficient adenosine diphosphate (ADP)-ribose binding module than macro domains from other CoVs. Furthermore, the crystal structure of the MERS-CoV macro domain was determined at 1.43-Å resolution in complex with ADP-ribose. Comparison of macro domains from MERS-CoV and other human CoVs revealed structural differences in the α1 helix alters how the conserved Asp-20 interacts with ADP-ribose and may explain the efficient binding of the MERS-CoV macro domain to ADP-ribose. This study provides structural and biophysical bases to further evaluate the role of the MERS-CoV macro domain in the host response via ADP-ribose binding but also as a potential target for drug design.

Since the severe acute respiratory syndrome (SARS)[2] outbreak in 2003 (1, 2), a newly discovered disease, Middle East respiratory syndrome (MERS), has been spreading from countries in the Middle East to America (3–5). In the summer of 2015, MERS was reported in North East Asia (6–8). The causative agent of MERS was identified as an unknown coronavirus (CoV) resembling SARS-CoV and referred to as Middle East respiratory syndrome CoV (MERS-CoV) (9–12). MERS-CoV belongs to the genus *Betacoronavirus* and possesses a positive-strand RNA genome that encodes viral proteins essential to the life cycle of the virus (13, 14). The mortality of MERS is 4-fold higher than SARS (40% compared with 10%) (15). Since the first case report in Saudi Arabia, MERS has been reported in more than 20 countries and has caused more than 400 deaths worldwide (9).

CoVs utilize the RNA genome to encode structural proteins, including spike glycoprotein (S), membrane protein (M), and nucleocapsid protein (N). They encode a large number of non-structural proteins (NSPs) for rapid replication. A single large replicase gene encodes all proteins involved in viral replication. The replicase gene contains two open reading frames (ORFs), ORF1a and ORF1b, which encode two polyproteins, pp1a and pp1ab; production of pp1ab requires a ribosomal frameshift to transcribe the portion encoded by ORF1b (16). ORF1a encodes viral proteases, main protease (M[pro], also called 3CL[pro]), and papain-like protease (PL[pro]), which are responsible for cleavage of the ORF1a and ORF1b gene products to produce functional NSPs.

In SARS-CoV, the largest NSP member, NSP3, is a multido-main protein containing the following domains: N-terminal acidic domain, macro domain, SARS-unique domain, PL[pro], nucleic acid-binding domain, marker domain (G$_2$M), transmembrane domain, and Y-domain (17). The MERS-CoV genome contains 16 NSPs (Fig. 1); except for 3CL[pro] and PL[pro] (18, 19), most of the functional domains within the NSP3 in MERS-CoV remain structurally uncharacterized.

The macro domain is named after the non-histone motif of the histone variant macroH2A, in which it was originally characterized (20–22), a protein module ubiquitous in eukaryotes, bacteria, and archaea. This domain is well known for its affinity to adenosine diphosphate (ADP)-ribose (23–25). Many cellular enzymes bearing macro domains within their structures interact with poly(ADP)-ribose (26–29). Poly(ADP)-ribosylation is a post-translational modification linked with DNA repair, apoptosis, gene regulation, and protein degradation. Thus, macro domain-containing proteins and enzymes may play important roles in regulating various cellular processes (30). Surprisingly, the CoVs studied so far and a few other viruses such as alphavirus, rubella virus, and hepatitis E virus possess macro domains in their genomes (16). In addition, some viral macro domains were found to have ADP-ribose 1″-phosphate phosphatase (ADRP) activity (31–33), which catalyzes the removal of phosphate from ADP-ribose 1″-phosphate (Appr1p) to produce ADP-ribose. ADRP activity has been reported in a yeast
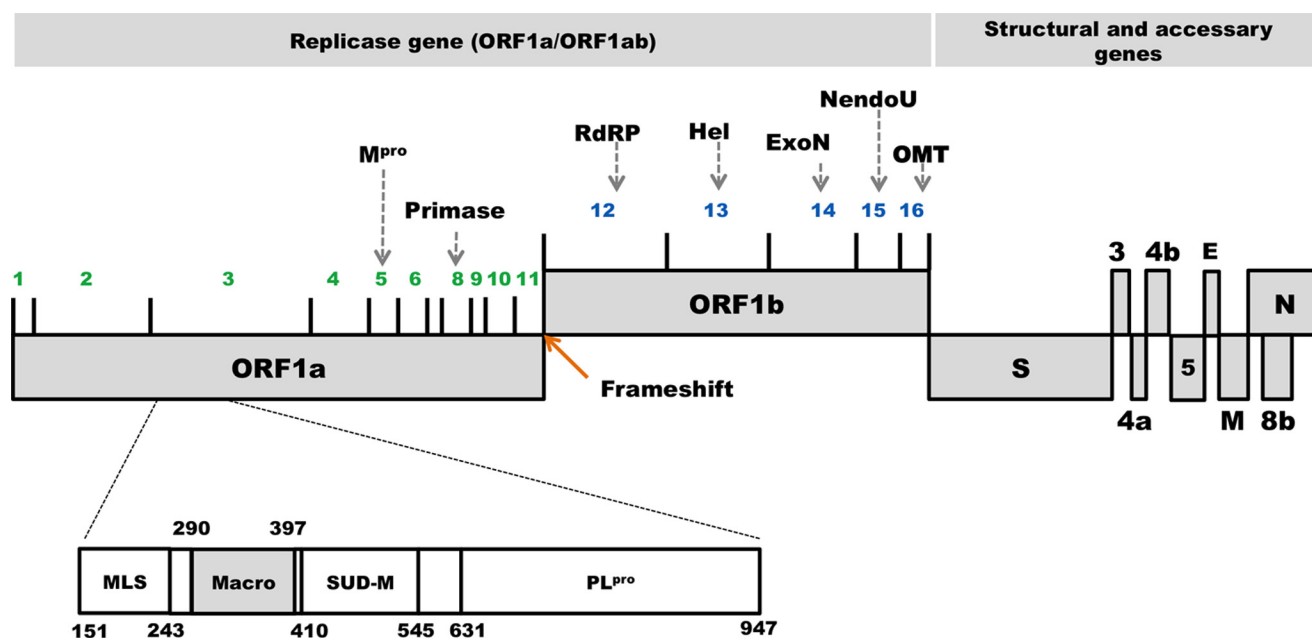
FIGURE 1. **Genome organization of MERS-CoV.** Schematic diagram of the composition of structural and non-structural proteins (*NSPs*) in MERS-CoV genome. Functional domains of NSP3 are highlighted. *M*pro, main (or 3CL) protease; *RdRp*, RNA-dependent RNA polymerase; *Hel*, helicase; *ExoN*, exoribonuclease; *NendoU*, endoribonuclease; *OMT*, 2′-O-methyltransferase; *S*, spike protein; *E*, envelope protein; *M*, membrane protein; *N*, nucleocapsid protein; *MLS*, mitochondira localization signal; *Macro*, macro domain; *SUD-M*, SARS-unique domain-M subdomain; *PL*pro, papain-like protease. NSPs encoded by ORF1a and ORF1b are numbered in *green* and *blue*, respectively.

protein containing macro domain as well as AF1521 protein in *Archaeoglobus fulgidus* (23, 34, 35). The enzymatic activity of viral macro domains in processing Appr1p is low (33, 36–38) and appears to be dispensable for virus RNA synthesis (31). In addition, the mutant for the CoV mouse hepatitis virus A59 (MHV-A59), encoding a single amino acid substitution of a strictly conserved residue for ADRP activity, replicated to slightly reduced titers in mouse liver but, strikingly, did not induce liver disease (39). The MHV macro domain exacerbates MHV-induced liver pathology, most likely by inducing excessive inflammatory cytokine expression. It was also reported that catalytic residues Asn-809, His-812, Gly-816, and Gly-817 for ADRP activity in hepatitis E virus macro domain are critical for hepatitis E virus replication (40). Accordingly, the development of drugs targeting the viral macro domain may be a strategy for antiviral therapy.

The macro domain of SARS-CoV NSP3 was previously reported to possess ADP-ribose and poly(ADP)-ribose binding ability, which suggests that the macro domain may regulate cellular proteins involved in an apoptotic pathway via poly-(ADP)-ribosylation to mediate the host response to infection (36). Structural studies of macro domains from CoVs such as human CoV 229E (HCoV-229E) and feline CoV (FCoV) also revealed interactions with ADP-ribose (41–43) and have offered huge advances in our understanding of viral macro domains. The MERS-CoV genome features a macro domain embedded in NSP3 (Fig. 1). However, we lack structural and functional information regarding the MERS-CoV macro domain.

In the present study, we investigated the MERS-CoV macro domain as an ADP-ribose binding module, with comparison to previously characterized viral macro domains. Furthermore, we determined the crystal structure of the MERS-CoV macro

domain in complex with ADP-ribose. Structural comparison of MERS-CoV and other human CoVs revealed divergence in ADP-ribose binding by macro domains. Our study may shed new light on structurally based design of novel antiviral drugs targeting viral macro domains.

Experimental Procedures

Protein Expression and Purification—The DNA sequence containing the MERS-CoV macro domain was synthesized by a local biotechnology company (MDBio, Inc.) and cloned into the pUC57 plasmid. The macro domain fragment was inserted between the NdeI and XhoI sites of the pET28a vector system (Novagen). The forward and reverse PCR primers used for amplification were macro-F (5′-AATTCATATGCCACTGA-GCAATTTTGAACA-3′) and macro-R (5′-AATTCTCGAGT-TAGATGGTCAGGCTCTTATAC-3′). The resulting plasmid with the inserted sequence was transformed into *Escherichia coli* BL21(DE3) cells, which were grown at 37 °C up to A_{600} 1.0 with 50 μg/ml of kanamycin. The expression of the recombinant MERS-CoV macro domain with an His tag at the N terminus was induced in cells with 1 mM isopropyl β-D-thiogalactoside, followed by growth for 20 h at 16 °C. Cells were collected by centrifugation and resuspended in lysis buffer (25 mM phosphate buffer, pH 7.0, 100 mM NaCl). After 20 min of sonication, the cell extract was clarified by centrifugation at 18,900 × *g* for 30 min at 4 °C to remove debris. The clear supernatant was placed in an open column filled with nickel-nitrilotriacetic acid resin. The resin was washed with 10 times volume of lysis buffer containing 50 and 100 mM imidazole, respectively. The His-tagged MERS-CoV macro domain was eluted by lysis buffer containing 300 mM imidazole. The purified MERS-CoV macro domain was dialyzed against stabilization buffer (25 mM phosphate buffer, pH 7.0, 100 mM NaCl, 0.5 mM dithiothreitol). The

His tag was removed by using thrombin, which resulted in four additional residues (GSHM) at the N terminus. The protein was further purified by gel filtration chromatography with a Superdex75 XK 16/60 column (GE Healthcare) in 20 mM Tris-HCl buffer (pH 7.0), 100 mM NaCl.

Circular Dichroism (CD) Spectroscopy—Far-UV CD spectra were measured with 10 μM protein samples in CD buffer (20 mM phosphate buffer, pH 3.5–8.5) placed into a 1-mm path length cuvette and recorded on a JASCO J-810 spectropolarimeter equipped with a Peltier temperature control system (JASCO International Co.). Thermal transition of protein samples with or without preincubation of 1 mM ADP-ribose were monitored at 220 nm from 25 to 95 °C at a scan rate of 1 °C/min. Baseline subtraction, smoothing, and data normalization involved the use of SigmaPlot. The melting temperature (T_m) was calculated with the maximum of the first derivative of the CD signal.

Differential Scanning Fluorimetry (DSF)—Thermal shift assay with DSF involved use of a CFX48 Real-time PCR Detection System (Bio-Rad). In total, a 25-μl mixture containing 2 μl of SYPRO Orange (Sigma), 1.25 μl of dialysis buffer (20 mM Tris-HCl, and 100 mM NaCl, pH 7.0), 10 μl of 1 μM protein sample, and various concentrations of ADP-ribose were mixed on ice in an 8-well PCR tube. Fluorescent signals were measured from 25 to 95 °C in 0.1 °C/30-s steps (excitation, 450–490 nm; detection, 560–580 nm). The main measurements were carried out in triplicate. Data evaluation and T_m determination involved use of the Bio-Rad CFX Manager, and data fitting and dissociation constant (K_d) calculations involved the use of SigmaPlot.

Isothermal Titration Calorimetry (ITC)—Binding of ADP-ribose to the MERS-CoV macro domain was measured by ITC with the Nano Isothermal Titration Calorimeter (TA Instruments). Aliquots of 3 μl of 1.14 mM ADP-ribose were titrated by injection into protein (0.057 mM in 0.98 ml) in 20 mM Tris-HCl (pH 7.0) and 100 mM NaCl. Experiments were carried out at 25 °C with 250 rpm stirring. Background heat from ligand to buffer titrations was subtracted, and the corrected heat from the binding reaction was used to derive values for the stoichiometry of the binding (n), K_d, apparent enthalpy of binding (ΔH), and entropy change (ΔS). Data were fitted by use of an independent binding model with Launch NanoAnalyze version 2.3.6.

Crystallization and Data Collection—The MERS-CoV macro domain and ADP-ribose were mixed in a molar ratio of 1:15. Initial protein crystallization trials were performed at 283 K by the sitting-drop vapor-diffusion method with commercial crystallization screen kits, 96-well Intelli-plates (Art Robbins Instruments), and a HoneyBee 963 robot (Genomic Solutions). Each crystallization drop was prepared by mixing 0.3 μl of macro domain/ADP-ribose at 10 mg/ml with an equal volume of mother liquor, and the mixture was equilibrated against 100 μl of reservoir solution. The crystals for data collection were grown in 1 week at 283 K with the optimal condition of 100 mM phosphate/citrate (pH 4.2), 2.0 M ammonium sulfate, and 10 mM nicotinamide adenine dinucleotide as the additive. For subsequent anomalous phasing, the crystal was soaked for 8 h in 3 mM mercuric(II) chloride, cryoprotected in mother liquor sup-

TABLE 1

Data collection and refinement statistics of MERS-CoV macro domain in complex with ADP-ribose

Crystal parameters		
Crystal	Hg-SAD	Native
Space group	$C222_1$	$C222_1$
Unit cell parameters		
a, b, c (Å)	41.4; 120.8; 66.7	41.8; 120.8; 67.7
α, β, γ (°)	90, 90, 90	90, 90, 90
Monomers per asymmetric unit cell	1	1
Data collection		
Wavelength (Å)	0.99347	1.00545
Resolution range (Å)	26.51–1.73 (1.79–1.73)	22.53–1.43 (1.48–1.43)
Unique No. of reflections	17,591	31,889
Total No. of reflections	229,930	186,275
I/σ^a	43.7 (4.5)	37.2 (6.8)
$R_{merge}^{a,b}$ (%)	6.7 (49.1)	2.9 (25.1)
Completeness^a (%)	99.1 (98.7)	99.8 (100.0)
Redundancy^a	13.1 (12.6)	5.8 (5.8)
$CC_{1/2}^{a,c}$	0.989 (0.953)	0.993 (0.972)
CC_{ano}^d	0.63	
Anomalous redundancy^a	6.9 (6.6)	
Anomalous completeness^a (%)	98.9 (98.6)	
Refinement statistics		
Resolution (Å)		1.43
R_{work} (%)/R_{free} (%)^e		12.73 / 16.19
R.m.s. deviation		
Bonds (Å)		0.007
Angles (°)		1.213
Mean B-factor (Å^2)		20.6
Protein		17.2
ADP-ribose		37.6
Water		36.3
Ramachandran plot (%)		
Favored		93.8
Allowed		6.2
Outliers		0.0

^{a} Values in parentheses are for the highest resolution shell.

^{b} $R_{merge} = \Sigma_h\Sigma_i|I_{h,i}-I_h|/\Sigma_h\Sigma_iI_{h,i}$, where I_h is the mean intensity of the i observations of symmetry related reflections of h.

^{c} $CC_{1/2}$ is a percentage of correlation between intensities from random half-datasets (56).

^{d} CC_{ano} is a percentage of correlation between random half-datasets of anomalous intensity differences.

^{e} $R_{work}/R_{free} = \Sigma|F_{obs} - F_{calc}|/\Sigma F_{obs}$, where F_{calc} is the calculated protein structure factor from the atomic model (R_{free} was calculated with 5% of the reflections selected).

plemented with 20% glycerol, and flash-frozen in liquid nitrogen at 100 K. The diffraction images were recorded in a 100-K nitrogen gas stream with use of BL13B1 or BL13C1 beamlines (National Synchrotron Radiation Research Center, Taiwan) and processed by using HKL2000 software (44).

Structure Determination and Refinement—The crystal structure of the MERS-CoV macro domain in complex with ADP-ribose was solved by the mercury(II) derivative single-wavelength anomalous dispersion method by using SHELXD/SHELXE software (45). The initial model was refined by the maximum likelihood method implemented in REFMAC5 (46) as part of the CCP4 suite (47) and rebuilt interactively by inspecting the σ-weighted electron density maps with coefficients $2mF_o - DF_c$ and $mF_o - DF_c$ in COOT (48). During the later stages, restrained positional and B-factor refinement involved the program phenix.refine (49). Water molecules were manually added at the final stages. The models were evaluated with use of PROCHECK (50) and MOLPROBITY (51). The data collection and structure refinement statistics are in Table 1.

Results and Discussion

ADP-ribose Binding Ability of MERS-CoV Macro Domain—The MERS-CoV macro domain (pp1a residues 1110 to 1273) was expressed and purified from *E. coli*. The final purified pro-
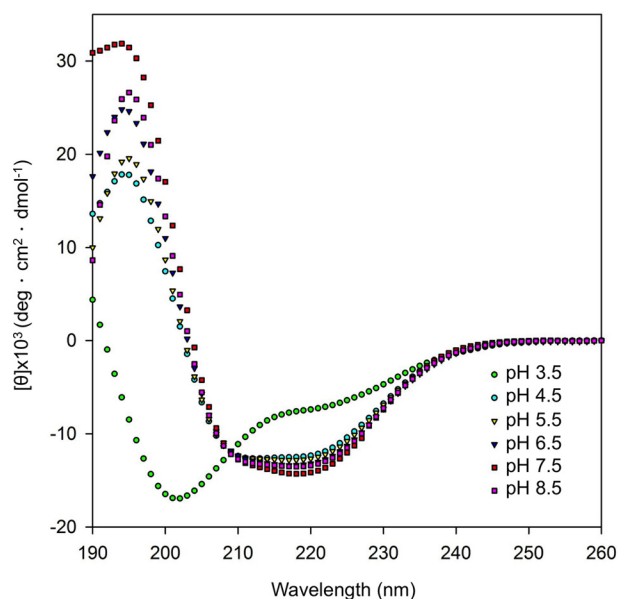
FIGURE 2. **Folding of MERS-CoV macro domain.** The CD spectra were recorded at 25 °C with 10 μM MERS-CoV macro domain in CD buffer (20 mM phosphate buffer, pH 3.5– 8.5) from 260 to 190 nm.

tein was a 167-amino acid protein (20 kDa), with four additional residues at the N terminus resulting from removal of the hexahistidine tag after thrombin cleavage. CD spectra revealed that the macro domain exhibited a stable α/β-type folding pattern under various pH conditions (Fig. 2). The T_m of the macro domain from thermal transition monitored by CD was 43 °C. However, the addition of ADP-ribose significantly increased the T_m to 51 °C (Fig. 3A). The significant increase in T_m suggests the interaction between the MERS-CoV macro domain and ADP-ribose.

To understand the affinity of ADP-ribose binding to the MERS-CoV macro domain, both DSF and ITC measurements were used to examine the equilibrium dissociation constant (K_d) of ADP-ribose. After fitting DSF data, the K_d was determined to be 3.12 ± 0.42 μM ($r^2 = 0.9628$) (Fig. 3B), which is similar to the calculated K_d of 2.95 μM based on ITC data (Fig. 3C). In addition, ITC data indicated that ADP-ribose bound to the MERS-CoV macro domain with favorable enthalpy change (exothermic, $\Delta H = -91.04$ KJ/mol). The binding reaction was spontaneous at 25 °C with exergonic Gibbs energy of binding ($\Delta G = -31.56$ KJ/mol). The thermodynamic profile ($\Delta G < 0$, $\Delta H < 0$, and $-T\Delta S > 0$) of ADP-ribose binding to the MERS-CoV macro domain suggests that ADP-ribose is likely stabilized by hydrogen bond formations (52).

We reviewed the results of previously reported binding assays of ADP-ribose binding to CoV macro domains (Table 2). Compared with the K_d of ADP-ribose binding to macro domains of human CoVs such as SARS-CoV (24 μM) (36) and HCoV-229E (28.9 μM) (41) and animal coronaviruses such as FCoV ($\sim$400 μM) (42), our K_d of 2.95 μM from biochemical analysis suggests that the MERS-CoV macro domain is a more efficient ADP-ribose binding module. The SARS macro domain possesses poly(ADP)-ribose binding ability and may play a role in the host response to virus (36). We found that the MERS-CoV macro domain interacts with ADP-ribose, which suggests

further investigating the role of the macro domain in MERS-CoV infection.

Overall Structure of MERS-CoV Macro Domain in Complex with ADP-ribose—We determined the crystal structure of ADP-ribose-bound MERS-CoV macro domain for further molecular elucidation. The orthorhombic crystals gave good quality x-ray diffraction and belonged to the space group C222$_1$ with the following unit cell dimensions: $a = 41.798$ Å, $b = 120.807$ Å, $c = 67.659$ Å, and $\alpha = \beta = \gamma = 90°$. The structure of the MERS-CoV macro domain was solved by mercury single-wavelength anomalous dispersion (see "Experimental Procedures"). The final protein structure (Fig. 4A) was refined to 1.43-Å resolution with R-factor and R-free values of 0.1273 and 0.1619, respectively (Table 1). The core of the structure of MERS-CoV macro domain is a seven-stranded β-sheet in the order of $\beta1$-$\beta2$-$\beta7$-$\beta6$-$\beta3$-$\beta5$-$\beta4$ (Fig. 4B). The central β-sheet is sandwiched between six α-helices, with $\alpha1$, $\alpha2$, and $\alpha3$ packing onto one face and $\alpha4$, $\alpha5$, and $\alpha6$ onto the other. In the initial refinement cycle, a strong bent electron density (continuous at 1σ cutoff) (Fig. 4A) located at the central pocket, was unambiguously identified as an ADP-ribose molecule. This molecule is tightly bound in an uncharged crevice located at the C-terminal end of strands $\beta3$ and $\beta6$ in the loop regions between $\beta3$-$\alpha2$ and $\beta6$-$\alpha5$ (Fig. 4A).

A search of the DALI database (53) with the structure of the MERS-CoV macro domain in complex with ADP-ribose used as a model revealed several structural homologs. Top-ranked structures were macro domains of CoVs in complex with ADP-ribose such as those for SARS-CoV (PDB code 2FAV; Z score 27.9; r.m.s. deviation 1.3; sequence identity 45%; sequence similarity 65%) (36), HCoV-229E (PDB code 3EWR; Z score 22.8; r.m.s. deviation 1.8; sequence identity 33%; sequence similarity 56%) (43), FCoV (PDB code 3JZT, Z score 22.6; r.m.s. deviation 1.8; sequence identity 30%; sequence similarity 53%) (42), and infectious bronchitis virus (PDB code 3EWP; Z score 19.5; r.m.s. deviation 1.9; sequence identity 28%; sequence similarity 47%) (43). This finding reflects that the viral macro domains are structurally well conserved. However, variability between all these structures arises from the loops connecting the core secondary structure elements, which display great diversity in sequence, length, and conformation and may correspond to different ADP-ribose binding ability.

Molecular Basis of ADP-ribose Binding in MERS-CoV Macro Domain—To gain insights into the molecular mechanism of ADP-ribose binding, we further investigated the binding pocket for ADP-ribose in the MERS-CoV macro domain. The adenine moiety resides in the hydrophobic cavity containing Gly-19, Ala-21, Ile-47, Pro-123, Leu-124, and Val-152 (Fig. 5A). Coordination of ADP-ribose involves serial hydrogen bond formations and hydrophobic interactions provided by surrounding amino acid residues (Fig. 5B). The side chain of Asp-20 contacts the N-6 atom of the pyrimidine ring in adenine moiety via direct hydrogen bonding. This residue is critical for binding specificity of the macro domain AF1521 in *A. fulgidus* (54). Structure-based multiple sequence alignment showed that this aspartic acid is conserved among CoV macro domains (Fig. 6A). Oxygen atoms of the pyrophosphate in ADP-ribose contact surrounding residues via hydrogen bonding with nitrogen
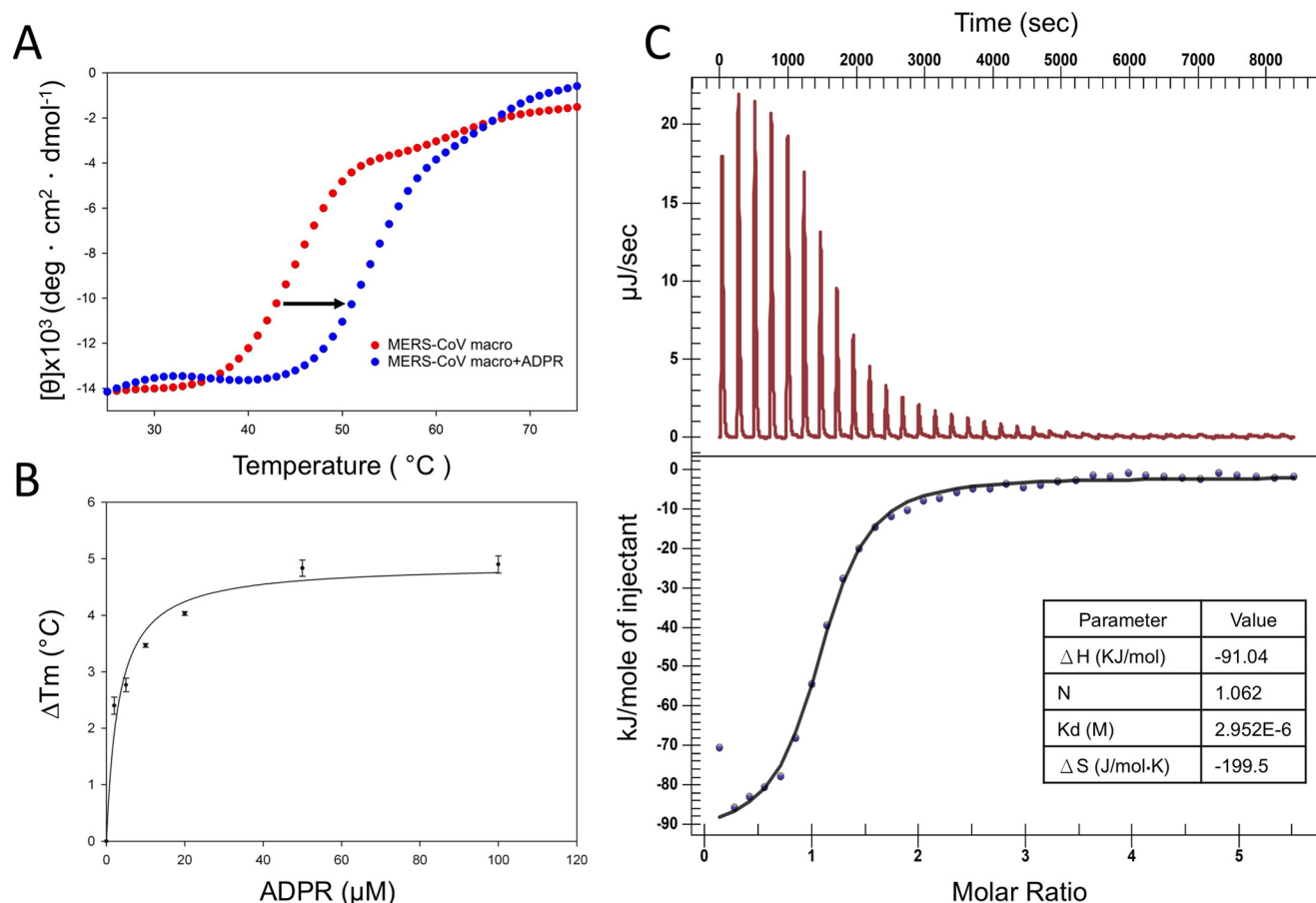
FIGURE 3. **ADP-ribose binding of MERS-CoV macro domain.** *A,* thermal denaturation of MERS-CoV macro domain. CD spectra were recorded at 220 nm with 10 μM MERS-CoV macro domain in CD buffer (20 mM phosphate buffer, pH 7.5) from 25 to 95 °C. The scatterplot shows the MERS-CoV macro domain with and without preincubation with 1 mM ADP-ribose, in *blue* and *red*, respectively. The melting temperature (T_m) was calculated by using the maximum of the first derivative of the CD signal; the *black arrow* indicates the shift of T_m. *B,* differential scanning fluorimetry of MERS-CoV macro domain by thermal shift assay on incubation with increasing concentrations of ADP-ribose. Data are mean $\pm$ S.E. from 3 independent experiments. Data were fitted by the means of 3 independent experiments. *C,* isothermal titration calorimetry analysis of ADP-ribose binding to MERS-CoV macro domain. *Upper panel,* raw data in μJ/s *versus* time showing heat release on injection of 1.14 mM ADP-ribose into a 980-μl cell containing 0.057 mM MERS-CoV macro domain. *Lower panel,* integration of raw data yielding the heat per mole *versus* molar ratio. The *inset* shows thermodynamic parameters of the experiment.

TABLE 2

Binding assays of ADP-ribose in CoV macro domains

Virus	Method	K_d	ΔH	ΔS	$-T\Delta S$	ΔG	References
		μM	KJ/mol	J/mol·K	KJ/mol		
MERS-CoV	ITC	2.95	−91.04	−199.5	59.48	−31.56	This study
	DSF	3.12					This study
SARS-CoV	ITC	24	−73.39	−153.9	46.65	−26.74	36
HCoV-229E	ITC	28.9	−14.54	38.1	−11.36	−25.9	41
FCoV	Pull-down based binding assay	~400					42

atoms in backbone amides of Ile-47, Ser-126, Gly-128, Ile-129, and Phe-130. The second ribose is stabilized by complex hydrogen bonding with surrounding residues and water molecules (Fig. 5*A*). The ribose-3″ oxygen atom forms a hydrogen bond with a nitrogen atom in the side chain of Asn-38. The ribose-2″ oxygen atom forms hydrogen bonds with the oxygen and nitrogen atoms in the backbone amides of Lys-42 and Gly-44, respectively. The ribose-1″ oxygen atom forms a hydrogen bond with the nitrogen atom in the backbone amide of Gly-46. A water molecule serves as a bridge between the ribose-1″ oxygen atom, Asn-38, and His-43. This organization of the terminal ribose and surrounding molecules was also observed in the yeast ADRP enzyme (34), which suggests that Asn-38 and His-43 may be critical for the hydrolysis reaction of ADP-ribose

1″-phosphate to ADP-ribose. In addition, equivalent residues critical for ADRP activity in the SARS-CoV macro domain (36) included Asn-35, Asn-38, His-43, Gly-44, Gly-45, and Phe-130, which are conserved in the MERS-CoV macro domain (Fig. 6*A*). Conservation of catalytically significant residues of ADRP in the MERS-CoV macro domain indicates that the MERS-CoV macro domain may possess ADRP enzymatic activity.

Structural Comparison of Macro Domains in MERS-CoV, SARS-CoV, and HCoV-229E—The structures of the macro domains of other CoVs pathogenic to humans, including SARS-CoV (36) and HCoV-229E (43), have been determined. Superposition of structures of MERS-CoV, SARS-CoV, and HCoV-229E macro domains shows that the major structural divergence lies in the $\alpha 1$ helices, which participates in stabili-
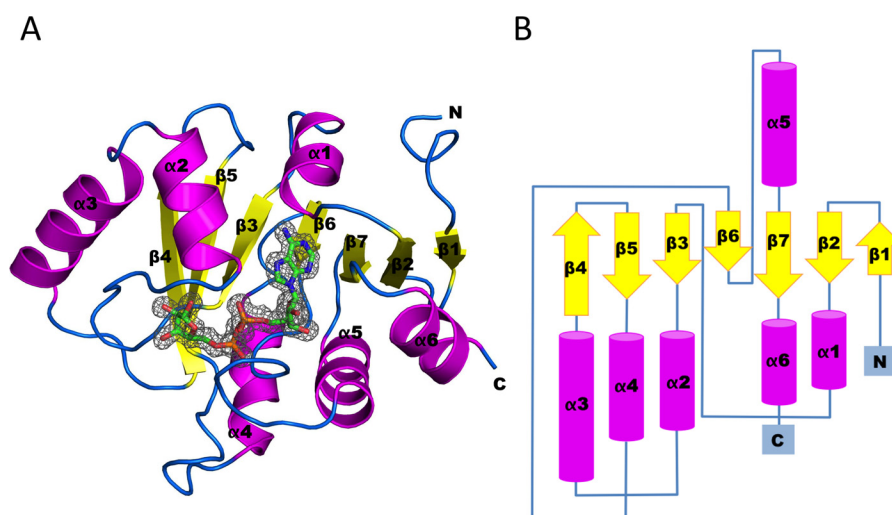
FIGURE 4. **Overall structure of MERS-CoV macro domain in complex with ADP-ribose.** *A,* structure of the MERS-CoV macro domain is represented by a ribbon model with helices, strands, and loops in *magenta*, *yellow*, and *blue*, respectively. ADP-ribose is displayed in sticks with carbon in *green*, oxygen in *red*, nitrogen in *blue*, and phosphorus in *orange*. The $2F_o - F_c$ difference map, contoured at 1σ, was calculated at 1.43-Å resolution from a model with the ligand omitted. *B,* topology diagram of MERS-CoV macro domain with the same colors as with ribbon representation.
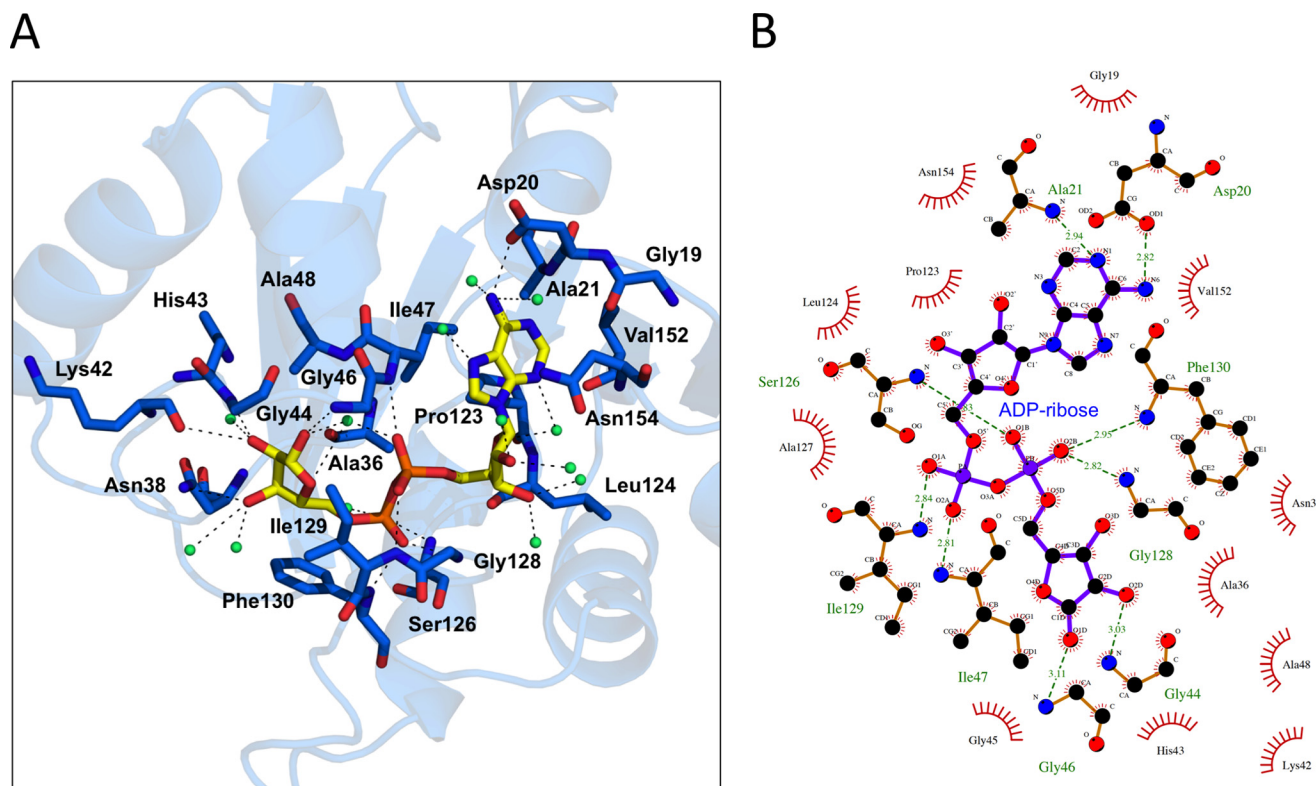
FIGURE 5. **Detailed view of ADP-ribose binding site in MERS-CoV macro domain.** *A,* a close-up of interactions in MERS-CoV macro domain with ADP-ribose binding. Amino acids and ADP-ribose are shown as sticks with carbon in *marine blue* and *yellow*, respectively; oxygen in *red*; nitrogen in *blue*; and phosphorus in orange. Water molecules are shown as *green spheres*. Hydrogen bonds are *black dashed lines*. *B,* interactions between MERS-CoV macro domain and ADP-ribose. Interactions between MERS-CoV macro domain and ADP-ribose were generated by using LigPlot[+] (55). ADP-ribose and surrounding residues are shown as ball-and-stick models with carbon in *black*, nitrogen in *blue*, oxygen in *red*, and phosphorus in *purple*. Atomic bonds in ADP-ribose and the MERS-CoV macro domain are in *purple* and *yellow*, respectively. Residues contacting ADP-ribose via hydrogen bonds are highlighted in *green* with hydrogen bonds shown as *dashed lines* and bond length as *numeric numbers*. Residues that provide hydrophobic interactions with ADP-ribose are in *black* with *red eyelash symbols*.

zation of ADP-ribose (Fig. 6*B*). Of note, in terms of the ADP-ribose binding pockets of the three structures, the structures of ADP-ribose appear at different degrees of curvature at the adenine moieties. In the MERS-CoV macro domain, the side chain of Asp-20 contacting ADP-ribose points into the cavity that holds adenine moiety. In the SARS-CoV macro domain, the

side chain position of the equivalent residue, Asp-23, varies significantly from that of Asp-20 in the MERS-CoV macro domain. This variation in side chain positions for Asp residues may result from different compositions of amino acids in the α1 helix. In the MERS-CoV macro domain, Asp-20 forms two hydrogen bonds with the N-6 atom in a pyrimidine ring of
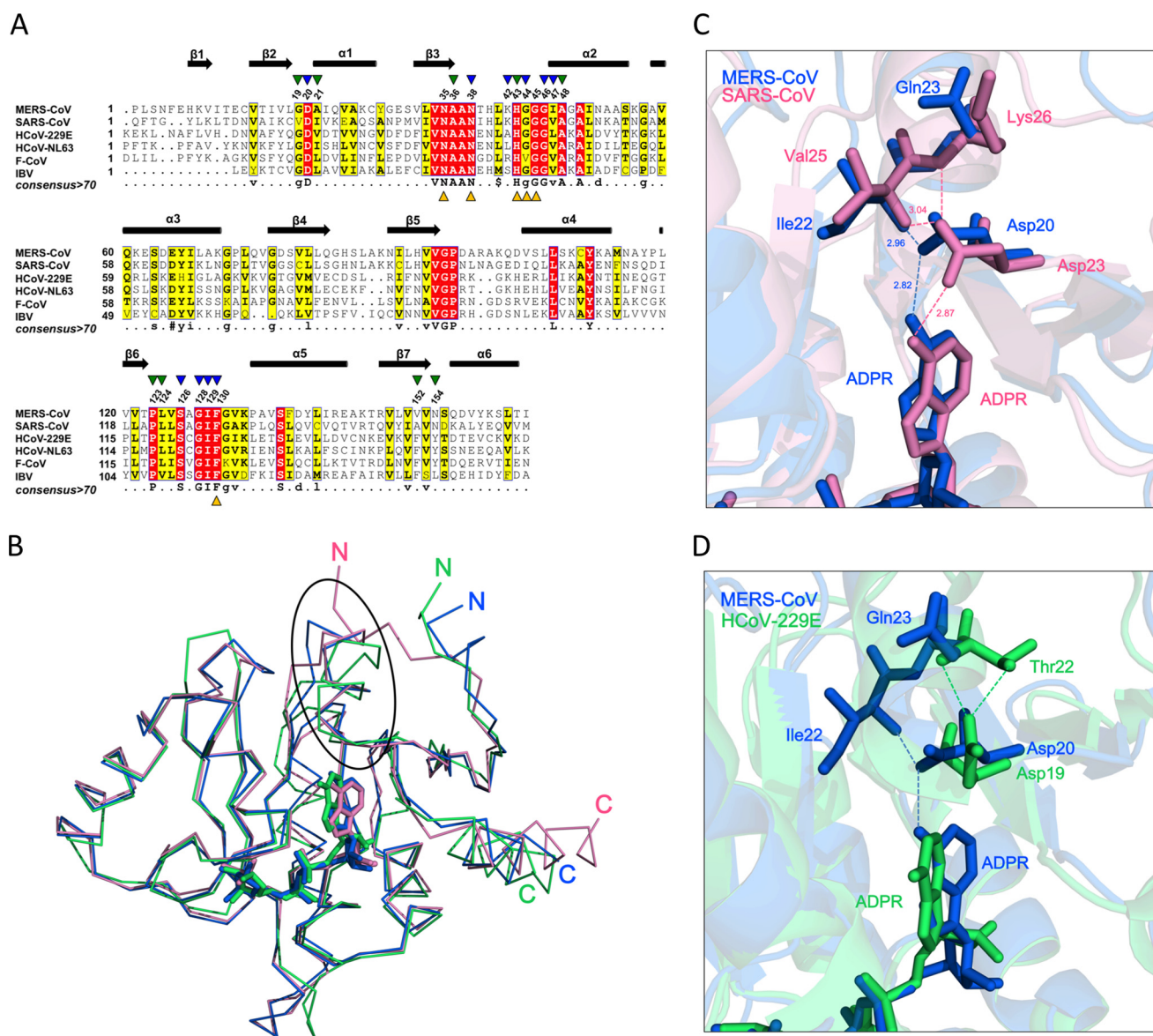
FIGURE 6. **Structural comparison of MERS-CoV, SARS-CoV, and HCoV-229E macro domains.** *A,* structure-based sequence alignment of CoV macro domains. Shown are MERS-CoV (PDB code 5DUS); SARS-CoV (PDB code 2FAV); human coronavirus 229E (HCoV-229E; PDB code 3EWR); HCoV-NL63 (PDB code 2VRI); and feline CoV (FCoV; PDB code 3JZT); and infectious bronchitis virus (*IBV*; PDB code 3EWP). Secondary structures of MERS-CoV macro domain are depicted on the *top* of the alignment with *arrows* for β strands and *cylinders* for α helices. Consensus amino acids among macro domains in CoVs with similarity score >0.7 are framed in *yellow* and depicted at the *bottom* of the alignment. Identical amino acids are in *white* and framed in *red*. *Blue* and *green arrowheads* on the top indicate amino acids forming hydrogen bonds and providing hydrophobic interactions with ADP-ribose, respectively. *Yellow arrowheads* at the bottom indicate equivalent amino acids in SARS-CoV macro domain found to abolish or decrease ADRP enzymatic activities when mutated. The number of residues corresponding to the MERS-CoV macro domain indicated by *blue, green,* and *yellow arrowheads* is shown on the top of the alignment. *B,* superposition of macro domains. Structures are shown as a ribbon model with MERS-CoV in *blue,* SARS-CoV in *pink,* and HCoV-229E in *green.* ADP-ribose molecules are shown as a stick model. Structural divergence is *circled with a black oval. C,* comparison of interactions in the adenine cavity of MERS-CoV and SARS-CoV macro domains. Amino acids and ADP-ribose are shown as a stick model. Hydrogen bonds are shown as *dashed lines* and bond lengths are indicated in Å units. *D,* comparison of interactions in adenine cavities of MERS-CoV and HCoV-229E macro domains. Amino acids and ADP-ribose are shown as a *stick model.* Hydrogen bonds are shown as *dashed lines.*

ADP-ribose and nitrogen in the Ile-22 backbone amide in the α1 helix via the same oxygen atom on its side chain, thereby dragging the Asp-20 side chain into the adenine cavity. In contrast, in the SARS-CoV macro domain, Asp-23 forms a hydrogen bond with the N-6 atom of adenine via one of the oxygen atoms in its side chain and with nitrogen atoms in Val-25 and Lys-26 backbone amides via another. Hydrogen bonding with Val-25 and Lys-26 of Asp-23 in the SARS-CoV macro domain causes a variation in side chain orientation from that for Asp-20 in the MERS-CoV macro domain. Furthermore, in the MERS-

CoV macro domain, the lengths of hydrogen bonds formed by the Asp-20 side chain with Ile-22 and ADP-ribose are 2.96 and 2.82 Å, respectively. In the SARS-CoV macro domain, the lengths of hydrogen bonds formed by the Asp-23 side chain with Val-25 and ADP-ribose are 3.04 and 2.87 Å, respectively (Fig. 6C). The differential strength of hydrogen bonds formed by Asp with ADP-ribose and residues in the α1 helix of the MERS-CoV and SARS-CoV macro domains may result from the presence of different residues in α1 helices that cause variations in side chain orientation of Asp residues in both struc-

tures. As compared with Asp-20 in MERS-CoV and Asp-23 in SARS-CoV, the equivalent residue in HCoV-229E is Asp-19, which does not contact ADP-ribose. Instead of forming a hydrogen bond directly with ADP-ribose, the side chain of Asp-19 in HCoV-229E contacts Thr-22 in the α1 helix via hydrogen bonding with oxygen and nitrogen atoms in the side chain and backbone of Thr-22, respectively. Hydrogen bonding with Thr-22 drags the side chain of Asp-19 in the HCoV-229E macro domain away from the adenine cavity as compared with the position of Asp-20 in the MERS-CoV macro domain (Fig. 6D). Consistent with the previous study, the thermodynamic profile ($\Delta G < 0$, $\Delta H < 0$, and $-T\Delta S < 0$) of ADP-ribose binding to the HCoV-229E macro domain suggests less contribution of the hydrogen bond to stabilization of ADP-ribose (41) (Table 2). Variations in strength of the hydrogen bond and orientation of the side chain in Asp residues may result in differential binding affinities of ADP-ribose observed in macro domains of MERS-CoV (K_d 2.95 μM), SARS-CoV (K_d 24 μM) (36), and HCoV-229E (K_d 28.9 μM) (41). The relationship between binding affinities of ADP-ribose in macro domains and differential pathogenicity of human CoVs needs further investigation.

Conclusion—Taken together, our biochemical study shows higher binding affinity for ADP-ribose in the MERS-CoV macro domain than macro domains of CoVs characterized to date. Structural analysis revealed that differences in the context of hydrogen bonds formed by the conserved Asp with ADP-ribose and residues in α1 helices in macro domains of MERS-CoV, SARS-CoV, and HCoV-229E may result in differential binding affinities for ADP-ribose. Our studies provide a biochemical basis for further investigating the role of macro domain in MERS-CoV infection and also the precise structural information for the design of novel antiviral drugs.

Author Contributions—C. H. H. conceived the study. C. C. C. and M. H. L. performed purification of the enzyme, biochemical assays, DSF, ITC, and crystallization. C. C. C., M. H. L., and C. Y. C. collected x-ray data. C. C. C. and C. H. H. determined and analyzed the crystal structure. C. C. C. and C. H. H. contributed to the manuscript writing. All authors reviewed the results and approved the final version of the manuscript.

References

1. Hui, D. S., Chan, M. C., Wu, A. K., and Ng, P. C. (2004) Severe acute respiratory syndrome (SARS): epidemiology and clinical features. *Postgrad. Med. J.* **80,** 373–381
2. Shaw, K. (2006) The 2003 SARS outbreak and its impact on infection control practices. *Public Health* **120,** 8–14
3. Kossyvakis, A., Tao, Y., Lu, X., Pogka, V., Tsiodras, S., Emmanouil, M., Mentis, A. F., Tong, S., Erdman, D. D., and Antoniadis, A. (2015) Laboratory investigation and phylogenetic analysis of an imported Middle East respiratory syndrome coronavirus case in Greece. *PloS One* **10,** e0125809
4. Rasmussen, S. A., Gerber, S. I., and Swerdlow, D. L. (2015) Middle East respiratory syndrome coronavirus: update for clinicians. *Clin. Infect. Dis.* **60,** 1686–1689
5. Thabet, F., Chehab, M., Bafaqih, H., and Al Mohaimeed, S. (2015) Middle East respiratory syndrome coronavirus in children. *Saudi Med. J.* **36,** 484–486
6. Dyer, O. (2015) South Korea scrambles to contain MERS virus. *BMJ* **350,** h3095
7. Hui, D. S., Perlman, S., and Zumla, A. (2015) Spread of MERS to South Korea and China. *Lancet Respir. Med.* **3,** 509–510
8. Park, S. Y., Kim, H. J., Yoo, K. H., Park, Y. B., Kim, S. W., Lee, S. J., Kim, E. K., Kim, J. H., Kim, Y. H., Moon, J. Y., Min, K. H., Park, S. S., Lee, J., Lee, C. H., Park, J., Byun, M. K., Lee, S. W., Rlee, C., Jung, J. Y., and Sim, Y. S. (2015) The efficacy and safety of prone positioning in adults patients with acute respiratory distress syndrome: a meta-analysis of randomized controlled trials. *J. Thorac. Dis.* **7,** 356–367
9. Banik, G. R., Khandaker, G., and Rashid, H. (2015) Middle East respiratory syndrome coronavirus "MERS-CoV": current knowledge gaps. *Paediatr. Respir. Rev.* **16,** 197–202
10. Han, H. J., Wen, H. L., Zhou, C. M., Chen, F. F., Luo, L. M., Liu, J. W., and Yu, X. J. (2015) Bats as reservoirs of severe emerging infectious diseases. *Virus Res.* **205,** 1–6
11. Jalal, S. (2015) The emerging threat of MERS. *J. Pak. Med. Assoc.* **65,** 310–311
12. Zaki, A. M., van Boheemen, S., Bestebroer, T. M., Osterhaus, A. D., and Fouchier, R. A. (2012) Isolation of a novel coronavirus from a man with pneumonia in Saudi Arabia. *New Engl. J. Med.* **367,** 1814–1820
13. Corman, V. M., Eckerle, I., Bleicker, T., Zaki, A., Landt, O., Eschbach-Bludau, M., van Boheemen, S., Gopal, R., Ballhause, M., Bestebroer, T. M., Muth, D., Muller, M. A., Drexler, J. F., Zambon, M., Osterhaus, A. D., Fouchier, R. M., and Drosten, C. (2012) Detection of a novel human coronavirus by real-time reverse-transcription polymerase chain reaction. *Euro Surveill.* **17,** pii, 20285
14. Geng, H., and Tan, W. (2013) A novel human coronavirus: Middle East respiratory syndrome human coronavirus. *Sci. China Life Sci.* **56,** 683–687
15. Zumla, A., Hui, D. S., and Perlman, S. (2015) Middle East respiratory syndrome. *Lancet* **386,** 995–1007
16. Snijder, E. J., Bredenbeek, P. J., Dobbe, J. C., Thiel, V., Ziebuhr, J., Poon, L. L., Guan, Y., Rozanov, M., Spaan, W. J., and Gorbalenya, A. E. (2003) Unique and conserved features of genome and proteome of SARS-coronavirus, an early split-off from the coronavirus group 2 lineage. *J. Mol. Biol.* **331,** 991–1004
17. Neuman, B. W., Joseph, J. S., Saikatendu, K. S., Serrano, P., Chatterjee, A., Johnson, M. A., Liao, L., Klaus, J. P., Yates, J. R., 3rd, Wüthrich, K., Stevens, R. C., Buchmeier, M. J., and Kuhn, P. (2008) Proteomics analysis unravels the functional repertoire of coronavirus nonstructural protein 3. *J. Virol.* **82,** 5279–5294
18. Lei, J., Mesters, J. R., Drosten, C., Anemüller, S., Ma, Q., and Hilgenfeld, R. (2014) Crystal structure of the papain-like protease of MERS coronavirus reveals unusual, potentially druggable active-site features. *Antiviral Res.* **109,** 72–82
19. Needle, D., Lountos, G. T., and Waugh, D. S. (2015) Structures of the Middle East respiratory syndrome coronavirus 3C-like protease reveal insights into substrate specificity. *Acta Crystallogr. D Biol. Crystallogr.* **71,** 1102–1111
20. Chakravarthy, S., Gundimella, S. K., Caron, C., Perche, P. Y., Pehrson, J. R., Khochbin, S., and Luger, K. (2005) Structural characterization of the histone variant macroH2A. *Mol. Cell. Biol.* **25,** 7616–7624
21. Kustatscher, G., Hothorn, M., Pugieux, C., Scheffzek, K., and Ladurner, A. G. (2005) Splicing regulates NAD metabolite binding to histone macroH2A. *Nat. Struct. Mol. Biol.* **12,** 624–625
22. Pehrson, J. R., and Fried, V. A. (1992) MacroH2A, a core histone containing a large nonhistone region. *Science* **257,** 1398–1400
23. Karras, G. I., Kustatscher, G., Buhecha, H. R., Allen, M. D., Pugieux, C., Sait, F., Bycroft, M., and Ladurner, A. G. (2005) The macro domain is an

ADP-ribose binding module. *EMBO J.* **24,** 1911–1920

24. Martzen, M. R., McCraith, S. M., Spinelli, S. L., Torres, F. M., Fields, S., Grayhack, E. J., and Phizicky, E. M. (1999) A biochemical genomics approach for identifying genes by the activity of their products. *Science* **286,** 1153–1155

25. Neuvonen, M., and Ahola, T. (2009) Differential activities of cellular and viral macro domain proteins in binding of ADP-ribose metabolites. *J. Mol. Biol.* **385,** 212–225

26. Miwa, M., and Sugimura, T. (1971) Splitting of the ribose-ribose linkage of poly(adenosine diphosphate-robose) by a calf thymus extract. *J. Biol. Chem.* **246,** 6362–6364

27. Oka, S., Kato, J., and Moss, J. (2006) Identification and characterization of a mammalian 39-kDa poly(ADP-ribose) glycohydrolase. *J. Biol. Chem.* **281,** 705–713

28. Slade, D., Dunstan, M. S., Barkauskaite, E., Weston, R., Lafite, P., Dixon, N., Ahel, M., Leys, D., and Ahel, I. (2011) The structure and catalytic mechanism of a poly(ADP-ribose) glycohydrolase. *Nature* **477,** 616–620

29. Ueda, K., Oka, J., Naruniya, S., Miyakawa, N., and Hayaishi, O. (1972) Poly ADP-ribose glycohydrolase from rat liver nuclei, a novel enzyme degrading the polymer. *Biochem. Biophys. Res. Commun.* **46,** 516–523

30. Gibson, B. A., and Kraus, W. L. (2012) New insights into the molecular and cellular functions of poly(ADP-ribose) and PARPs. *Nat. Rev. Mol. Cell Biol.* **13,** 411–424

31. Putics, A., Filipowicz, W., Hall, J., Gorbalenya, A. E., and Ziebuhr, J. (2005) ADP-ribose-1″-monophosphatase: a conserved coronavirus enzyme that is dispensable for viral replication in tissue culture. *J. Virol.* **79,** 12721–12731

32. Putics, A., Gorbalenya, A. E., and Ziebuhr, J. (2006) Identification of protease and ADP-ribose 1″-monophosphatase activities associated with transmissible gastroenteritis virus non-structural protein 3. *J. Gen. Virol.* **87,** 651–656

33. Saikatendu, K. S., Joseph, J. S., Subramanian, V., Clayton, T., Griffith, M., Moy, K., Velasquez, J., Neuman, B. W., Buchmeier, M. J., Stevens, R. C., and Kuhn, P. (2005) Structural basis of severe acute respiratory syndrome coronavirus ADP-ribose-1″-phosphate dephosphorylation by a conserved domain of nsP3. *Structure* **13,** 1665–1675

34. Kumaran, D., Eswaramoorthy, S., Studier, F. W., and Swaminathan, S. (2005) Structure and mechanism of ADP-ribose-1″-monophosphatase (Appr-1″-pase), a ubiquitous cellular processing enzyme. *Protein Sci.* **14,** 719–726

35. Shull, N. P., Spinelli, S. L., and Phizicky, E. M. (2005) A highly specific phosphatase that acts on ADP-ribose 1″-phosphate, a metabolite of tRNA splicing in *Saccharomyces cerevisiae*. *Nucleic Acids Res.* **33,** 650–660

36. Egloff, M. P., Malet, H., Putics, A., Heinonen, M., Dutartre, H., Frangeul, A., Gruez, A., Campanacci, V., Cambillau, C., Ziebuhr, J., Ahola, T., and Canard, B. (2006) Structural and functional basis for ADP-ribose and poly(ADP-ribose) binding by viral macro domains. *J. Virol.* **80,** 8493–8502

37. Kuri, T., Eriksson, K. K., Putics, A., Züst, R., Snijder, E. J., Davidson, A. D., Siddell, S. G., Thiel, V., Ziebuhr, J., and Weber, F. (2011) The ADP-ribose-1″-monophosphatase domains of severe acute respiratory syndrome coronavirus and human coronavirus 229E mediate resistance to antiviral interferon responses. *J. Gen. Virol.* **92,** 1899–1905

38. Putics, A., Slaby, J., Filipowicz, W., Gorbalenya, A. E., and Ziebuhr, J. (2006) ADP-ribose-1″-phosphatase activities of the human coronavirus 229E and SARS coronavirus X domains. *Adv. Exp. Med. Biol.* **581,** 93–96

39. Eriksson, K. K., Cervantes-Barragán, L., Ludewig, B., and Thiel, V. (2008) Mouse hepatitis virus liver pathology is dependent on ADP-ribose-1″-phosphatase, a viral function conserved in the α-like supergroup. *J. Virol.*
82, 12325–12334

40. Parvez, M. K. (2015) The hepatitis E virus ORF1 "X-domain" residues form a putative macrodomain protein/Appr-1″-pase catalytic-site, critical for viral RNA replication. *Gene* **566,** 47–53

41. Piotrowski, Y., Hansen, G., Boomaars-van der Zanden, A. L., Snijder, E. J., Gorbalenya, A. E., and Hilgenfeld, R. (2009) Crystal structures of the X-domains of a Group-1 and a Group-3 coronavirus reveal that ADP-ribose-binding may not be a conserved property. *Protein Sci.* **18,** 6–16

42. Wojdyla, J. A., Manolaridis, I., Snijder, E. J., Gorbalenya, A. E., Coutard, B., Piotrowski, Y., Hilgenfeld, R., and Tucker, P. A. (2009) Structure of the X (ADRP) domain of nsp3 from feline coronavirus. *Acta Crystallogr. D Biol. Crystallogr.* **65,** 1292–1300

43. Xu, Y., Cong, L., Chen, C., Wei, L., Zhao, Q., Xu, X., Ma, Y., Bartlam, M., and Rao, Z. (2009) Crystal structures of two coronavirus ADP-ribose-1″-monophosphatases and their complexes with ADP-ribose: a systematic structural analysis of the viral ADRP domain. *J. Virol.* **83,** 1083–1092

44. Otwinowski, Z., and Minor, W. (1997) Processing of x-ray diffraction data collected in oscillation mode. *Method Enzymol.* **276,** 307–326

45. Sheldrick, G. M. (2010) Experimental phasing with SHELXC/D/E: combining chain tracing with density modification. *Acta Crystallogr. D Biol. Crystallogr.* **66,** 479–485

46. Murshudov, G. N., Vagin, A. A., and Dodson, E. J. (1997) Refinement of macromolecular structures by the maximum-likelihood method. *Acta Crystallogr. D. Biol. Crystallogr.* **53,** 240–255

47. Winn, M. D., Ballard, C. C., Cowtan, K. D., Dodson, E. J., Emsley, P., Evans, P. R., Keegan, R. M., Krissinel, E. B., Leslie, A. G., McCoy, A., McNicholas, S. J., Murshudov, G. N., Pannu, N. S., Potterton, E. A., Powell, H. R., Read, R. J., Vagin, A., and Wilson, K. S. (2011) Overview of the CCP4 suite and current developments. *Acta Crystallogr. D Biol. Crystallogr.* **67,** 235–242

48. Emsley, P., Lohkamp, B., Scott, W. G., and Cowtan, K. (2010) Features and development of Coot. *Acta Crystallogr. D Biol. Crystallogr.* **66,** 486–501

49. Adams, P. D., Afonine, P. V., Bunkóczi, G., Chen, V. B., Davis, I. W., Echols, N., Headd, J. J., Hung, L. W., Kapral, G. J., Grosse-Kunstleve, R. W., McCoy, A. J., Moriarty, N. W., Oeffner, R., Read, R. J., Richardson, D. C., Richardson, J. S., Terwilliger, T. C., and Zwart, P. H. (2010) PHENIX: a comprehensive Python-based system for macromolecular structure solution. *Acta Crystallogr. D Biol. Crystallogr.* **66,** 213–221

50. Laskowski, R. A., Macarthur, M. W., Moss, D. S., and Thornton, J. M. (1993) Procheck: a program to check the stereochemical quality of protein structures. *J. Appl. Crystallogr.* **26,** 283–291

51. Chen, V. B., Arendall, W. B., 3rd, Headd, J. J., Keedy, D. A., Immormino, R. M., Kapral, G. J., Murray, L. W., Richardson, J. S., and Richardson, D. C. (2010) MolProbity: all-atom structure validation for macromolecular crystallography. *Acta Crystallogr. D Biol. Crystallogr.* **66,** 12–21

52. Haq, I. (2002) Thermodynamics of drug-DNA interactions. *Arch. Biochem. Biophys.* **403,** 1–15

53. Holm, L., and Rosenström, P. (2010) Dali server: conservation mapping in 3D. *Nucleic Acids Res.* **38,** W545–549

54. Allen, M. D., Buckle, A. M., Cordell, S. C., Löwe, J., and Bycroft, M. (2003) The crystal structure of AF1521 a protein from Archaeoglobus fulgidus with homology to the non-histone domain of macroH2A. *J. Mol. Biol.* **330,** 503–511

55. Laskowski, R. A., and Swindells, M. B. (2011) LigPlot+: multiple ligand-protein interaction diagrams for drug discovery. *J. Chem. Inf. Model* **51,** 2778–2786

56. Karplus, P. A., and Diederichs, K. (2012) Linking crystallographic model and data quality. *Science* **336,** 1030–1033

Macro Domain from Middle East Respiratory Syndrome Coronavirus (MERS-CoV) Is an Efficient ADP-ribose Binding Module: CRYSTAL STRUCTURE AND BIOCHEMICAL STUDIES

Chao-Cheng Cho, Meng-Hsuan Lin, Chien-Ying Chuang and Chun-Hua Hsu

Access the most updated version of this article at doi: 10.1074/jbc.M115.700542

Alerts:
- When this article is cited
- When a correction for this article is posted

Click here to choose from all of JBC's e-mail alerts

This article cites 56 references, 17 of which can be accessed free at
http://www.jbc.org/content/291/10/4894.full.html#ref-list-1